ADVANCED OPTICAL MATERIALS
www.advopticalmat.de

Vertical Thermal Emission from Optical Antennas on an Epsilon-Near–Zero Substrate

*Irfan Khan, Milan Palei, Owen Dominguez, Evan Simmons, Viktor A. Podolskiy, and Anthony J. Hoffman**

This work presents a novel approach to achieve directional and normal thermal emission from epsilon-near–zero (ENZ) materials. ENZ materials exhibit near–zero permittivity at the ENZ point, resulting in some unique properties compared to conventional optical materials including infinite wavelength, constant phase distribution, and decoupling of spatial and temporal fields inside the ENZ material. These properties are used to engineer the far-field thermal emission from optical antennas fabricated on ENZ film in the mid-infrared. By coupling the antenna resonance mode with the Berreman mode of the ENZ material, highly directional and normal emission is demonstrated. This approach could have significant implications for thermal management, energy conversion, and sensing applications.

1. Introduction

Thermal emission is a fundamental process in which electromagnetic radiation is emitted by a material when it is heated above absolute zero. In this process the internal energy from the thermal reservoir is transferred spontaneously to photons in the radiation field.[1] This phenomenon, which is described by Planck's Law, states that for an ideal black body the spectral density of the emitted radiation is determined by its temperature. This emission is ubiquitous, broadband, omnidirectional, and in general assumed to be temporally and spatially incoherent in nature. Considerable progress has been made over the last decade to precisely engineer these properties of thermally emitted light using wavelength-scale optical structures.[2–5]

Directionality and normal emission are two key properties that determine the functionality of thermal emitters. Directionality refers to the ability of an object to emit light preferentially in a particular direction, whereas normal emission refers to the ability of an emitter to emit perpendicular to its surface. The ability to control the directionality of thermal emission enables a broad range of applications in sensing, energy harvesting and conversion, imaging, and spectroscopy, where efficient light collection and coupling are crucial.[6–9] Due to the omni-directional nature of thermal emission, most of the emitted energy is wasted by radiating in unwanted directions, resulting in poor collection efficiency. Therefore, the development of thermal sources with the ability to control the emission direction is of fundamental importance.

Controlling directivity of thermal emitters is challenging due to the fundamental limits imposed by thermodynamics and the complex interplay between the emitter's geometry, material properties, and surrounding environment.[2] Thermal emission from any material is characterized by its emissivity—which is the measure of an object's ability to emit thermal radiation relative to an ideal black body. According to Kirchhoff's law of thermal radiation, at any given temperature and wavelength, the spectral directional emittance from an object is equal to the spectral absorptance for radiation incident from the same direction. This complimentary relationship between emission and optical absorption suggests that the optical properties of thermal emission can be engineered by nano-structuring or careful material selection.

Over the years, many techniques have been proposed to achieve directional thermal emission, including plasmonic nanostructures, surface-phonon polariton gratings, magneto-optical lattice resonances, photonic crystals, hyperbolic metamaterials, and metasurfaces.[10–16] These approaches, however, have limitations in terms of spectral selectivity, narrow bandwidths, and emission in oblique directions only. An alternative approach in controlling the directivity is using thin film made of materials exhibiting epsilon-near–zero (ENZ) behavior. These materials support a leaky polarized electromagnetic mode known as the Berreman mode, which can couple with free-space modes at specific angles of incidence.[17] However, this angular response is limited to narrowband frequencies, and oblique directions only. Broadband, directional thermal emission from ENZ materials in oblique angles have been realized by sandwiching multiple oxides and graded doped III–V semiconductors with multiple ENZ points.[18,19]

I. Khan, M. Palei, O. Dominguez[+], A. J. Hoffman
Department of Electrical Engineering
University of Notre Dame
Notre Dame, IN 46556, USA
E-mail: ajhoffman@nd.edu

E. Simmons, V. A. Podolskiy
Department of Physics and Applied Physics
University of Massachusetts
Lowell, MA 01854, USA

The ORCID identification number(s) for the author(s) of this article can be found under https://doi.org/10.1002/adom.202400715

[+]Present address: Los Alamos National Laboratory, Los Alamos, NM 87544, USA

DOI: 10.1002/adom.202400715

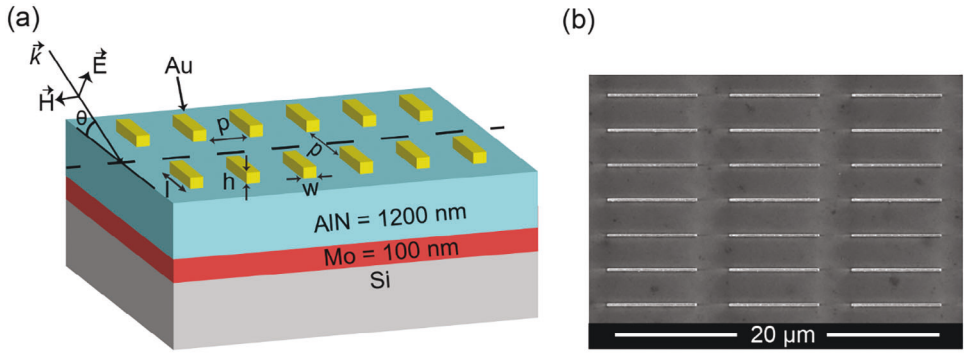

Figure 1. a) Schematic of the optical antennas patterned on the AlN/Mo/Si substrate. b) SEM image of a portion of the antenna array.

In this paper, we present a new approach to obtain directional and normal thermal emission from ENZ materials by patterning optical antennas on it. The optical response of plasmonic antennas placed on ENZ substrates has been investigated in prior studies in other contexts.[20–26] Our approach leverages the unique properties of ENZ materials, which exhibit near–zero permittivity near the ENZ point, to tailor the thermal emission of the antennas. The radiation pattern of an antenna fabricated on a substrate is pre-dominantly directed toward the medium with the higher refractive index.[26] For weakly dispersive positive permittivity substrates with $Re(\epsilon) > 1$, the field pattern is forward scattered into the substrate. In case of the ENZ substrate with $0 < Re(\epsilon) < 1$, the electromagnetic field is backscattered into the air.[27] As the $Re(\epsilon)$ approaches 0 at the ENZ wavelength, the electromagnetic energy is radiated in the direction normal to emitter's surface. Because of this reason, optical structures which can support electromagnetic modes at ENZ frequencies are of great interest. One such mode is the Berreman mode. The Berreman mode provides strong confinement and field enhancement in the ENZ film and is leaky at the air/ENZ interface.[28] By patterning periodic arrays of nano-bar antennas on the air/ENZ interface, we demonstrate coupling between the antenna resonance mode and the Berreman mode, which drastically modify the far-field radiation pattern. We demonstrate experimentally that our approach enables highly directional and normal emission, paving the way for new advances in thermal management, energy conversion, and sensing applications.

2. Experimental Section

Optical antenna arrays were fabricated on sub-wavelength layers of AlN with a metal ground plane. A 100 nm thick Mo ground plane was deposited on a Si carrier substrate followed by 1.2 μm of polycrystalline AlN deposited via sputtering. The wafers were diced into 1.2 × 1.2 cm^2 pieces, and 1 × 1 cm^2 antenna arrays were fabricated using electron beam lithography and metal liftoff.[29] A schematic of the sample and antenna arrays is shown in **Figure** 1a. Three antenna arrays comprising antennas of different lengths were used in this work. The dimensions of individual antennas in the three arrays were 120 nm wide, 90 nm thick, and 2.73, 4.77, and 8.27 μm long for samples 1, 2, and 3, respectively. For all of the arrays, the antennas were spaced 2 μm apart from their nearest neighbor. A scanning electron microscope (SEM) image of a portion of the antenna array for sample 2 is shown in Figure 1b.

Angle-, wavelength-, and polarization-dependent emission measurements were performed by collecting the angle-dependent emission from a heated sample. The optical setup for measuring thermal emission is shown in **Figure 2**. Samples were mounted with thermal paste and a clip to a custom heated rotating stage. The temperature of the heated stage was measured by a type K thermocouple bolted directly onto the stage just above the sample. For all of the measurements presented here, a stage temperature of 300 °C was used. Angle-dependent thermal emission from the sample was collimated using an uncoated Au parabolic mirror. A dual-layer leaf design iris was placed between the parabolic mirror and the sample to ensure that emission was collected only from the sample; the dual layer design mitigates heating of the iris from the stage and the resultant thermal emission from the side of the iris facing the sample. A beamsplitter with a flipping mount was used to direct light either to the Fourier transform infrared spectrometer (FTIR) or to a CMOS camera, which was used for alignment purposes. When measuring mid-infrared (mid-IR) spectra, the beam was routed through a pair of off-axis parabolic mirrors into the FTIR. A second iris was placed after the last parabolic mirror to control the width of the collimated beam entering the FTIR through the external port. A polarizer was placed between the second iris and the FTIR to select the polarization of the emitted light. For the transverse magnetic (TM) polarization, the sample was aligned such that the magnetic field was parallel to both the short axis of the bar antennas and the rotation axis of the heated stage as shown in the inset of Figure 2. A room-temperature deuterated triglycine sulfate detector with a CsI window was used for all the measurements.

The spectral emissivity of an antenna arrays was obtained by modifying the technique in Ref. [30] to include angle. This approach requires three spectra to be measured for each angle: 1) emission from the heated array, 2) emission from a heated grey body, and 3) baseline emission from the room temperature surroundings. The angle-dependent, spectral emissivity was then calculated using

$$\varepsilon\ (\lambda,\theta) = \left[\frac{S_s^{exp}(\lambda,\theta,T_s) - S_R^{exp}(\lambda,T_R)}{S_B^{exp}(\lambda,\theta,T_B) - S_R^{exp}(\lambda,T_R)}\right]\left[\frac{P(\lambda,T_B) - P(\lambda,T_R)}{P(\lambda,T_S) - P(\lambda,T_R)}\right] \quad (1)$$

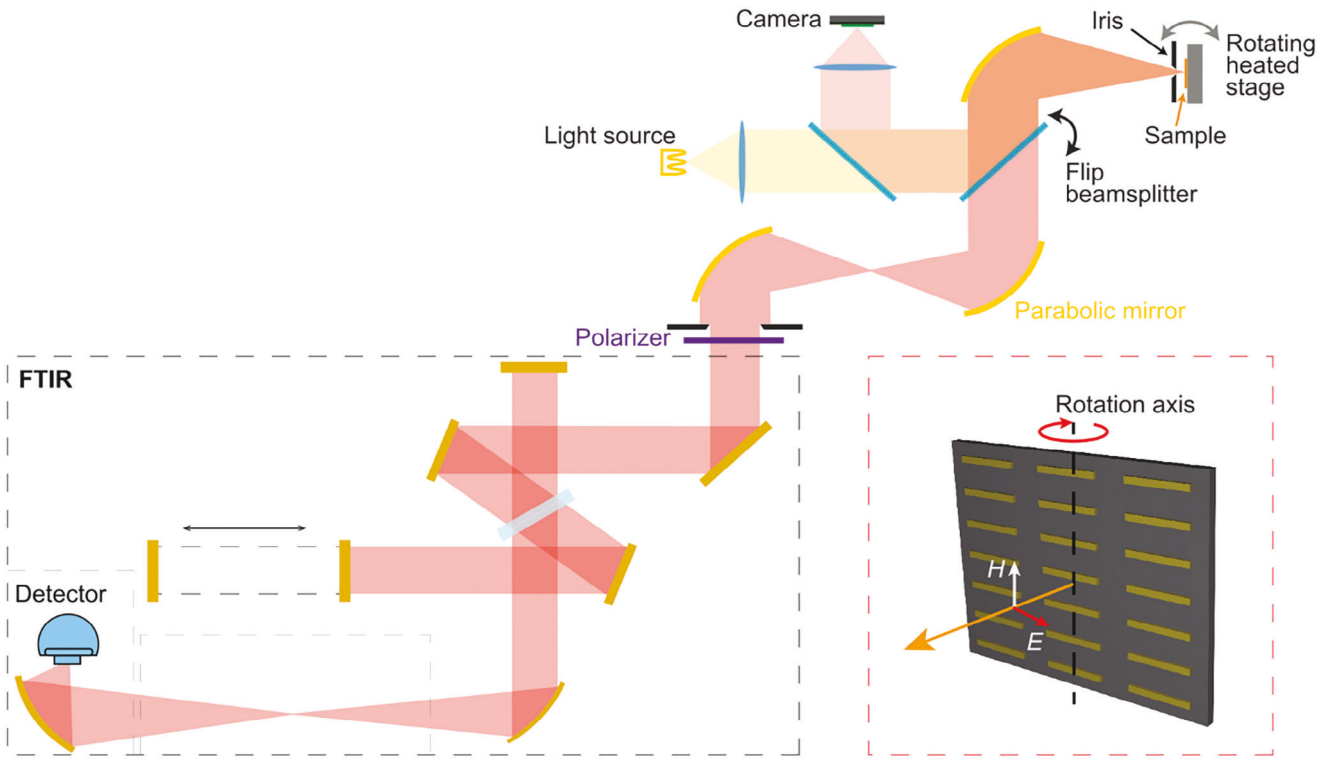

Figure 2. Optical setup for measuring the emissivity of Au antennas on ENZ substrate. The inset in the dashed red box shows the TM polarization of the emitted light. The $\vec{H}$ field is parallel to rotation axis of the stage and along the short axis of the bar antennas.

where, S_S^{exp} is the single channel emission from the sample at temperature T_S, S_B^{exp} is the heated blackbody emission at temperature T_B, S_R^{exp} is the background emission from the room temperature surroundings, and P is the Planck function. A Au-coated glass substrate covered with soot was used to measure S_B^{exp}; the dimensions of the substrate were the same as the samples. The soot was deposited by holding the gold coated substrate over a candle for 10 min. The thickness of the deposited soot was about 2 mm. The background emission, S_R^{exp}, was obtained by closing the dual-layer iris in front of the heater. Each measured spectrum was averaged over 50 scans with a spectral resolution of 4 cm^{-1} and an angular step of 1°.

Finite element simulations of the Si/Mo/AlN substrate with bar antennas patterned on it, were performed. The simulations were performed with COMSOL Multiphysics software with optical parameters of materials taken from literature.[31–34] Only a single unit cell of the structure with Floquet periodic boundaries was simulated as shown in **Figure 3**a. The TM polarization for the incident wave was used such that the magnetic field was along the short axis of the bar antenna.

2.1. Results and Discussions

Figure 3b shows the simulated angle dependent TM polarized absorption from the Si/Mo/AlN substrate without any antennas patterned on it. The strong absorption close to the LO phonon frequency of the AlN is due to the Berreman mode. There is no absorption from the Berreman mode at normal incidence.[35] As the angle of incidence increases, the Berreman mode blue-shifts and its FWHM broadens. The maximum absorption is observed at around 30° incidence, where the absorption coefficient is close to unity.

Next, we model the absorption for Au bar-antennas patterned on the Si/Mo/AlN substrate. The simulations are performed at normal incidence to eliminate absorption due to the Berreman mode and excite only the resonant modes of the antenna. The tuning of the antenna resonance with antenna length is shown in Figure 3c. The first order antenna resonant mode blue-shifts and broadens as the antenna length decreases. The dashed red line shows the spectral position of $\mathrm{Re}(\epsilon = 0)$ for AlN. We use this result as a guide to fabricate bar antennas on ENZ substrates with three different lengths such that, a) the first order antenna mode is far-away from the ENZ point, where $\mathrm{Re}(\epsilon_{AlN}) > 1$, b) in the vicinity of the ENZ point ($\mathrm{Re}(\epsilon_{AlN}) \sim 0$), and c) beyond the ENZ point where $Re(\epsilon_{AlN}) < 0$. These three regions are highlighted in blue, yellow, and red, respectively, in Figure 3c.

The measured TM polarized, angle-dependent spectral emissivity for the bare Si/Mo/AlN structure without any antennas is shown in **Figure 4**a. The colorscale shows the measured emissivity at 300 °C, while the overlaid circles show the incident-angle–dependent wavelength of the modes obtained from finite element simulations. The simulations are performed using room temperature dielectric permittivity, and does not account for the change in permittivity due to temperature. The slight red-shift in the measured emissivity is attributed to the softening of the optical phonons at elevated temperature.[36,37] This is attributed to the red-shift in the optical phonons at high temperature. The

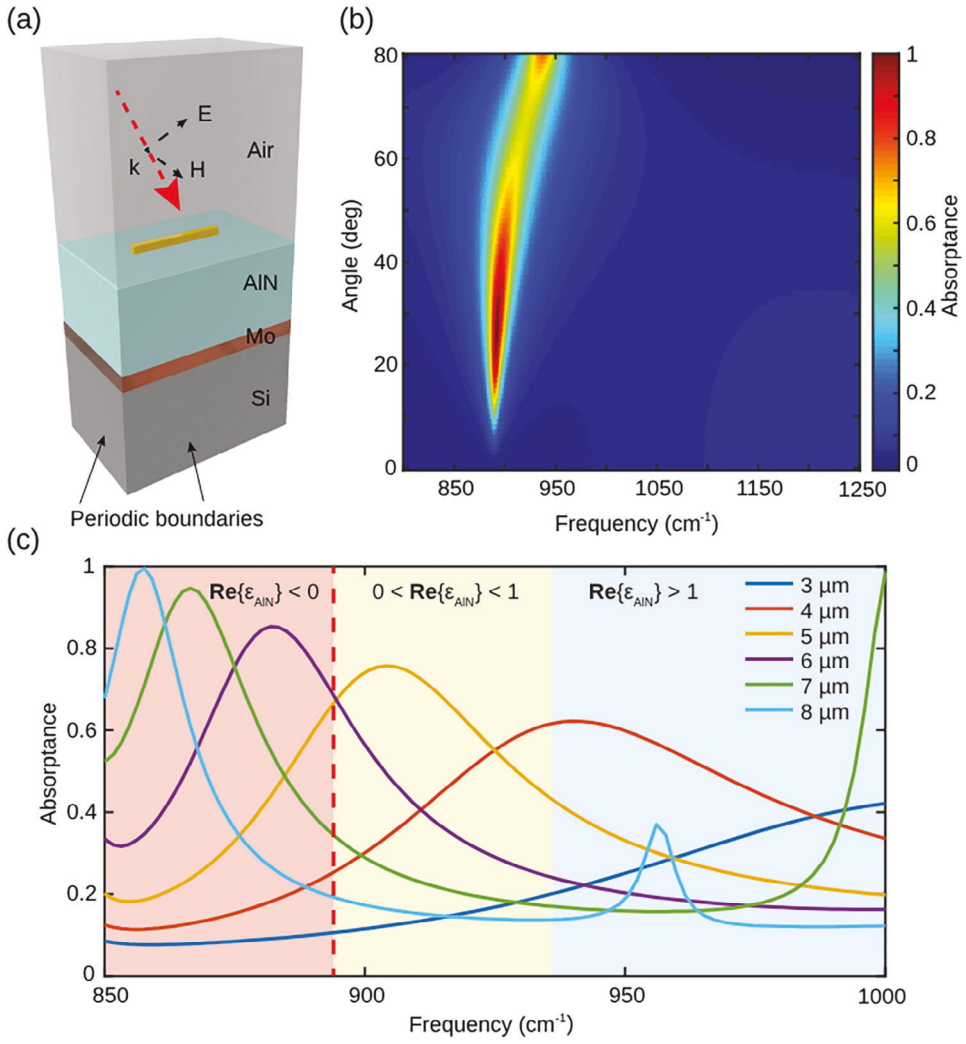

Figure 3. a) Schematic of unit cell for the finite element simulation. b) Absorption due to the Berreman mode of AlN calculated using TMM method. c) Tuning of first order antenna mode as a function of antenna length simulated using COMSOL.

spectral position of each mode is obtained by choosing the local maximum of the absorption peak for each simulated angle. We attribute the slight asymmetry with angle in the measured emissivity for all the samples to minor misalignment between the focus spot of the parabolic mirror and the rotational axis of the stage positioned at the surface of the sample.

For sample 1 (2.73 μm antenna array), the antenna modes are far-away from the ENZ region of the AlN substrate, where there is no coupling between the Berreman mode and the resonant modes of the bar-antenna. The measurements exhibit two strong spectral features that are readily identified as shown in Figure 4b. The narrow peak in emissivity around 885 cm^{-1} corresponds to increased emission from the leaky Berreman mode of the AlN thin film. The emissivity peaks at ≈30°, and the frequency of the mode blue-shifts with increasing angle. The first order antenna mode ($m = 1$), indicated by the black circles, is at 1088 cm^{-1} for normal emission. This mode exhibits some emission at 0°. and two dominant side lobes with maximum emission around 50°. from the normal. The emission blue-shifts as the angle increases from zero to peak emissivity at 50°, after which it starts to red-shift with increasing the angle.

For sample 2 (4.77 μm antenna array), the first order resonant mode of the bar-antenna is just to the high-frequency side of the ENZ region where $0 < Re(\epsilon_{AlN}) < 1$. The emissivity from this sample is shown in Figure 4c. For this sample the Berreman and first order antenna modes are observed at 880 and 922 cm^{-1}, respectively. Due to the coupling between these two modes, the Berreman mode is slightly red-shifted as compared to sample 1.[29] Also, the Berreman mode exhibits weak dispersion at small angles, and the red-shift is observed at higher angles only. The first order antenna mode has near unity emission between −40° to 40°. The dispersive mode between 950 and 1150 cm^{-1}, and the mode at 1250 cm^{-1} correspond to the second and third order antennas modes. These modes are beyond the scope of this study and are not discussed further.

When the resonant mode of the antenna is to the low frequency side of the Berreman mode, where $Re(\epsilon_{AlN}) < 0$, the angle-dependence of the thermal emission is strongly modified and

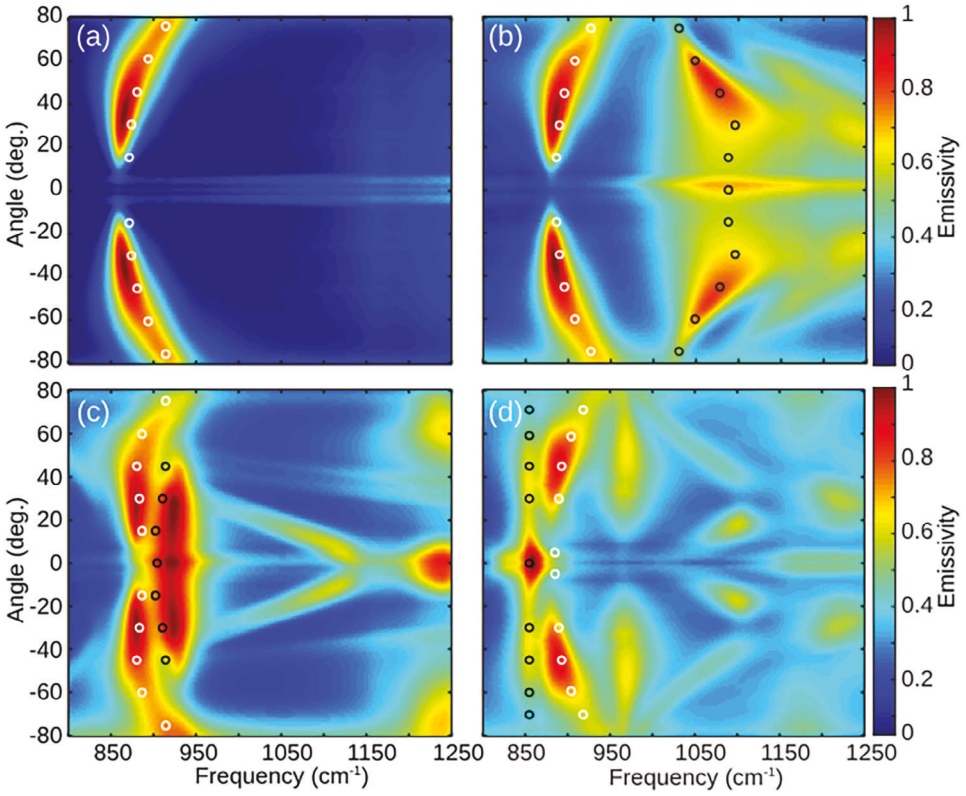

Figure 4. Measured normalized far-field thermal emission versus frequency and angle for Si/Mo/AlN multilayer structure with a) without any antennas, b) 2.73 μm antennas, c) 4.77 μm antennas, and d) 8.27 μm antennas. The white, and black circles show the peak position of Berreman mode, and first order antenna resonant modes, respectively, obtained from finite element simulations.

emission is into a narrow angular region about the normal as shown in Figure 4d for the 8.27 μm antennas. Similarly, the emission from the main lobes of the Berreman mode moves away from the normal to higher angles. We observe a small amount of normal emission from the Berreman mode, which is attributed to the excitation of the Berreman mode due to the light scattered by the antennas.[20] The antenna mode radiates into ±10° of the normal. The emission in the normal direction is due to the lower refractive index of the ENZ substrate than air. For an antenna at the interface of two dielectric media, the emission is directed toward the medium with higher refractive index, with the direction of the main beams at an angle related to $\sin^{-1}(n_1/n_2)$ from the normal, with n_1 and n_2 being the refractive indices of the substrate and superstrate, respectively.[38] As, the refractive index of the substrate becomes vanishingly small at the ENZ point, the main beams are directed in the normal direction.

Figure 5b,c shows a cross-section of simulated electric field profile ($E_{z\_}$ component) for the 2.73 and 8.27 μm antennas for $m = 1$ mode at normal incidence. The cross-section is taken along one of the short ends of the antennas. Here, we are plotting the field for three neighboring antennas for clarity purposes. The actual simulation was performed with periodic boundaries and with incident electric field polarized parallel to the length of the antennas. For the 2.73 μm antennas, there is no coupling between the neighboring antennas. For the 8.27 μm antennas long range coupling between neighboring antennas is observed. This is due to the antenna mode coupling to the Berreman mode, which has very long in-plane wavelength close to ENZ point. The Berreman mode can simultaneously couple multiple antennas, which translate to increased spatial coherence, and hence the reduced angular spread (≈4× reduction) as shown in Figure 5a.

To quantitatively evaluate the directionality of the different antenna arrays, we define a figure of merit ($FOM = \Delta E/\Delta\theta$), where ΔE is the contrast between maximum and minimum emissivity and $\Delta\theta$ is the angular spread and calculated as the FWHM of $E(\theta)$ at a specific frequency.[39] A high FOM value signifies better directionality. FOM value of 0.31, 0.49, and 1.75 is calculated for the $m = 1$ mode for the 2.73, 4.77, and 8.27 μm antenna arrays, respectively. The angular spread and angular contrast in Figure 5a can be improved by tuning the thickness of the AlN layer.

Significant spectral line width narrowing is also observed for the longer antennas. **Figure 6** shows the emissivity for the three antenna samples measured at 0° angle with electric field polarization along the length of the antenna. The peak position of first order mode for each antenna length is indicated by the arrow. The central peak position of FWHM of these modes are obtained by fitting Gaussian functions to the spectra in Figure 6. From the fitting, we calculate the central frequency of the first order antenna mode at 1085, 909, and 852 cm^{-1} for the 2.73, 4.77, and 8.27 μm antennas, respectively. The corresponding FWHM for the three antenna arrays are 32.9, 15.9, and 6.8 cm^{-1}, respectively. Shifting the resonant mode of the antenna close to the Berreman

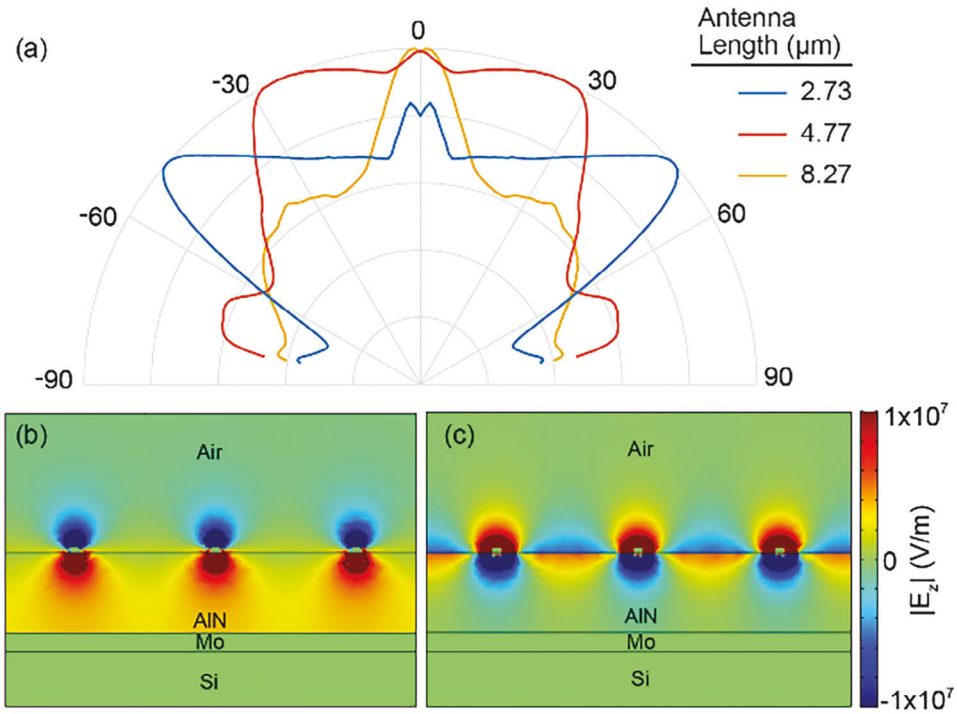

Figure 5. a) Far-field radiation plot for $m = 1$ mode for the three antenna arrays at 1088, 922, and 860 cm^{-1} respectively. b,c) Corresponding simulated electric field, $|E_z|$, profile for the 2.73 and 8.27 μm antenna arrays showing coupling between adjacent antennas.

mode, results in a spectral narrowing of 4.8× for the longest antennas. We also observe significant improvements in the *Q*-factor ($Q = \frac{\omega_{res}}{\Delta\omega}$) of the resonant mode. The *Q* factor increases from 31.2 for the 2.73 μm antenna to 125 for the 8.27 μm antenna array. This is an improvement of 4× in the *Q* factor. For the 8.27 μm antenna, we also observe a shoulder at 849 cm^{-1}. This is attributed to the excitation of the surface phonon polariton mode of the AlN layer.

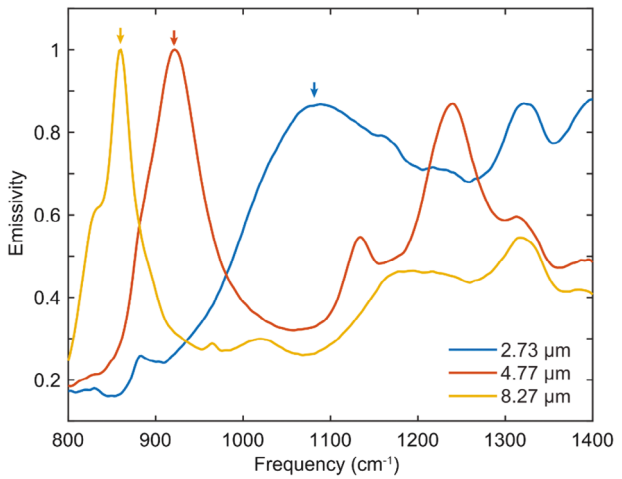

Figure 6. Thermal emissivity measured at normal angle to the surface. The position of the first order antenna mode ($m = 1$) is shown by the blue, red, and yellow arrows for 2.73, 4.77, and 8.27 μm antennas, respectively.

3. Conclusion

We demonstrate the effect of ENZ substrate on the far-field thermal emission of optical antennas. We fabricated bar antennas on ENZ substrate with three different lengths such that the frequency of first order resonant mode is, a) far-away from the ENZ point where the real part of permittivity of the substrate is positive and greater than 1, b) in the vicinity of the ENZ point, and c) beyond the ENZ point where the real part of permittivity is negative.

The ENZ substrate drastically modifies the far-field emission from the optical antennas. The first order antenna mode exhibits far-field emission that depends strongly on the length of the antenna. In general, as the antenna length is increased, the antenna modes redshift, couple to the Berreman mode, and spectrally pin as the modal index vanishes. At the same time, the direction of the thermal emission moves toward the normal. Coupling to the Berreman mode also results in spectral and spatial narrowing of the antenna mode. The work presented here could lead to new ways of engineering absorption, emission, and scattering in the mid- and far-infrared. The limited directional bandwidth may be an obstacle to practical applications, but it can be overcome using approaches like by using gradient heterostructures of different ENZ materials or multiple antennas of different lengths in a supercell.

Acknowledgements

This work was supported by the National Science Foundation (VP: NSF-DMREF-2118787).

Conflict of Interest

The authors declare no conflict of interest.

Author Contributions

The manuscript was written by I.K. and A.H. and includes contributions of all authors. All authors have given approval to the final version of the manuscript.

Data Availability Statement

The data that support the findings of this study are available from the corresponding author upon reasonable request.

Keywords

epsilon-near–zero, nanoantenna arrays, vertical thermal emission

Received: March 14, 2024
Revised: June 24, 2024
Published online: July 30, 2024

[1] R. M. Goody, X. Huang, in *Encyclopedia of Atmospheric Sciences*, G. R. North, J. Pyle, F. Zhang, 2nd ed., Elsevier, New York **2015**, pp. 5–12.
[2] D. G. Baranov, Y. Xiao, I. A. Nechepurenko, A. Krasnok, A. Alù, M. A. Kats, *Nat. Mater.* **2019**, *18*, 920.
[3] B. X. Wang, M. Q. Liu, T. C. Huang, C. Y. Zhao, *ES Energy Environ.* **2019**, 18;
[4] Z. Sakotic, A. Krasnok, N. Cselyuszka, N. Jankovic, A. Alú, *Phys. Rev. Appl.* **2020**, *13*, 064073.
[5] G. Lu, C. R. Gubbin, J. R. Nolen, T. Folland, M. J. Tadjer, S. De Liberato, J. D. Caldwell, *Nano Lett.* **2021**, *21*, 1831.
[6] W. Li, S. Fan, *Opt. Express* **2018**, *26*, 15995.
[7] C. Blanchard, Q. Lévesque, D. Costantini, C. Jamois, J. L. Leclercq, A. L. Coutrot, F. Marquier, L. Milord, C. Grillet, H. Benisty, P. Viktorovitch, X. Letartre, J.-J. Greffet, *Adv. Photonics* **2015**.
[8] Y. Qu, M. Pan, M. Qiu, *Phys. Rev. Appl.* **2020**, *13*, 064052.
[9] A. Lenert, D. M. Bierman, Y. Nam, W. R. Chan, I. Celanovic, M. Soljacic, E. N. Wang, *Nat. Nanotechnol.* **2014**, *9*, 126.
[10] J. H. Park, S. E. Han, P. Nagpal, D. J. Norris, *ACS Photonics* **2016**, *3*, 494.
[11] K. Shi, Y. Xing, Y. Sun, N. He, T. Guo, S. He, *Adv. Opt. Mater.* **2022**, *10*, 2201732.
[12] S. Campione, F. Marquier, J.-P. Hugonin, A. R. Ellis, J. F. Klem, M. B. Sinclair, T. S. Luk, *Sci. Rep.* **2016**, *6*, 34746.
[13] C. Blanchard, L. Wojszvzyk, C. Jamois, J.-L. Leclercq, C. Chevalier, L. Ferrier, P. Viktorovitch, I. Moldovan-Doyen, F. Marquier, J.-J. Greffet, X. Letartre, *Opt. Mater. Express* **2022**, *12*, 1.
[14] E. Ozbay, A. Ghobadi, B. Butun, H. Hajian, *Opt. Express* **2017**, *25*, 31970.
[15] K. Feng, G. Harden, D. L. Sivco, A. J. Hoffman, *Opt. Express* **2018**, *26*, 4382.
[16] A. Livingood, J. R. Nolen, T. G. Folland, L. Potechin, G. Lu, S. Criswell, J.-P. Maria, C. T. Shelton, E. Sachet, J. D. Caldwell, *ACS Photonics* **2021**, *8*, 472.
[17] S. Vassant, J. P. Hugonin, F. Marquier, J. J. Greffet, *Opt. Express* **2012**, *20*, 23971.
[18] A. P. Raman, J. Xu, J. Mandal, presented at Optica Advanced Photonics Congress 2022, Maastricht, Netherlands, July **2022**.
[19] J. Xu, J. Mandal, A. P. Raman, *Science* **2021**, *372*, 393.
[20] Y. C. Jun, J. Reno, T. Ribaudo, E. Shaner, J.-J. Greffet, S. Vassant, F. Marquier, M. Sinclair, I. Brener, *Nano Lett.* **2013**, *13*, 5391.
[21] K. Manukyan, M. Z. Alam, C. Liu, K. Pang, H. Song, Z. Zhao, M. Tur, R. W. Boyd, A. E. Willner, *Appl. Phys. Lett.* **2021**, *118*, 241102.
[22] M. Z. Alam, S. A. Schulz, J. Upham, I. De Leon, R. W. Boyd, *Nat. Photonics* **2017**, *12*, 79.
[23] S. A. Schulz, A. A. Tahir, M. Z. Alam, J. Upham, I. De Leon, R. W. Boyd, *Phys. Rev. A* **2016**, *93*, 063846.
[24] Y. Hou, L. Cheng, Z. Wen, T. Li, J. Mao, Y. Xu, F. Liu, J. Hao, W. Jiang, Y. Zhang, L. Zhang, *Opt. Laser Technol.* **2023**, *166*, 109538.
[25] C. T. DeVault, V. A. Zenin, A. Pors, K. Chaudhuri, J. Kim, A. Boltasseva, V. M. Shalaev, S. I. Bozhevolnyi, *Optica* **2018**, *5*, 1557.
[26] J. Kim, A. Dutta, G. V. Naik, A. J. Giles, F. J. Bezares, C. T. Ellis, J. G. Tischler, A. M. Mahmoud, H. Caglayan, O. J. Glembocki, A. V. Kildishev, J. D. Caldwell, A. Boltasseva, N. Engheta, *Optica* **2016**, *3*, 339.
[27] M. Memarian, G. V. Eleftheriades, *Prog. Electromagn. Res.* **2013**, *142*, 437.
[28] I. Khan, Z. Fang, M. Palei, J. Lu, L. Nordin, E. L. Simmons, O. Dominguez, S. M. Islam, H. G. Xing, D. Jena, V. A. Podolskiy, D. Wasserman, A. J. Hoffman, *Opt. Express* **2020**, *28*, 28590.
[29] O. Dominguez, L. Nordin, J. Lu, K. Feng, D. Wasserman, A. J. Hoffman, *Adv. Opt. Mater.* **2019**, *7*, 1800826.
[30] F. Marquier, K. Joulain, J. P. Mulet, R. Carminati, J. J. Greffet, Y. Chen, *Phys Rev B Condens Matter Mater Phys* **2004**, *69*, 155412.
[31] L. Nordin, O. Dominguez, C. M. Roberts, W. Streyer, K. Feng, Z. Fang, V. A. Podolskiy, A. J. Hoffman, D. Wasserman, *Appl. Phys. Lett.* **2017**, *111*, 091105.
[32] D. Chandler-Horowitz, P. M. Amirtharaj, *J. Appl. Phys.* **2005**, *97*, 123526.
[33] N. K. Grady, N. J. Halas, P. Nordlander, *Chem. Phys. Lett.* **2004**, *399*, 167.
[34] M. R. Querry, M. A. Ordal, R. J. Bell, L. L. Long, R. W. Alexander, *Appl. Opt.* **1985**, *24*, 4493.
[35] B. Harbecke, B. Heinz, P. Grosse, *Appl. Phys. A* **1985**, *38*, 263.
[36] X. B. Chen, J. Huso, J. L. Morrison, L. Bergman, A. P. Purdy, *J. Appl. Phys.* **2005**, *98*, 026106.
[37] A. Link, K. Bitzer, W. Limmer, R. Sauer, C. Kirchner, V. Schwegler, M. Kamp, D. G. Ebling, K. W. Benz, *J. Appl. Phys.* **1999**, *86*, 6256.
[38] N. Engheta, C. H. Papas, C. Elachi, *Radio Sci* **1982**, *17*, 1557.
[39] W. Qiuyu, L. Tianji, L. Longnan, H. Chen, W. Jiawei, X. Meng, Y. Li, W. Li, *Nanophotonics* **2024**, *13*, 793.